Conformational Heterogeneity at Position U37 of an All-RNA Hairpin Ribozyme with Implications for Metal Binding and the Catalytic Structure of the S-Turn[†,‡]

Shabnam Alam, Valerie Grum-Tokars,[§] Jolanta Krucinska, Melisa L. Kundracik,[||] and Joseph E. Wedekind*

Department of Biochemistry and Biophysics, University of Rochester School of Medicine and Dentistry, Rochester, New York 14642

Received August 3, 2005; Revised Manuscript Received September 10, 2005

ABSTRACT: The hairpin ribozyme is an RNA enzyme that performs site-specific phosphodiester bond cleavage between nucleotides A−1 and G+1 within its cognate substrate. Previous functional studies revealed that the minimal hairpin ribozyme exhibited "gain-of-function" cleavage properties resulting from U39C or U39 to propyl linker (C3) modifications. Furthermore, each "mutant" displayed different magnesium-dependence in its activity. To investigate the molecular basis for these gain-of-function variants, crystal structures of minimal, junctionless hairpin ribozymes were solved in native (U39), and mutant U39C and U39(C3) forms. The results revealed an overall molecular architecture comprising two docked internal loop domains folded into a wishbone shape, whose tertiary interface forms a sequestered active site. All three minimal hairpin ribozymes bound $Co(NH_3)_6^{3+}$ at G21/A40, the E-loop/S-turn boundary. The native structure also showed that U37 of the S-turn adopts both sequestered and exposed conformations that differ by a maximum displacement of 13 Å. In the sequestered form, the U37 base packs against G36, and its 2′-hydroxyl group forms a water mediated hydrogen bond to O4′ of G+1. These interactions were not observed in previous four-way-junction hairpin ribozyme structures due to crystal contacts with the U1A splicing protein. Interestingly, the U39C and U39(C3) mutations shifted the equilibrium conformation of U37 into the sequestered form through formation of new hydrogen bonds in the S-turn, proximal to the essential nucleotide A38. A comparison of all three new structures has implications for the catalytically relevant conformation of the S-turn and suggests a rationale for the distinctive metal dependence of each mutant.

The hairpin ribozyme is a member of the small ribozyme family that includes naturally occurring catalytic RNA motifs such as the hammerhead, VS, hepatitis-*δ*-virus, and metabolite sensing varieties (*2*, *3*). The hairpin ribozyme, like other family members, supports site-specific phosphodiester bond cleavage of a complementary substrate (*3*−*6*) leading to formation of a cyclic-2′,3′ phosphodiester bond and a free 5′-hydroxyl group as products (Figure 1A). The natural form of the hairpin ribozyme was identified in the (−)RNA strands of the satellite tobacco ringspot virus genome (*7*) and was shown to fold as a compact, X-shaped structure (*8*). Deletion analysis indicated that significant portions of the 4WJ[1] fold are dispensable for docking and catalysis (*9*). Two independently folding domains were identified with the discovery that the covalent bond between nucleotides 14 and 15 (Figure 1B) could be severed and that separate domains could be reconstituted to produce a minimal, junctionless hairpin ribozyme (*10*, *11*). Whereas the steady state cleavage rate of the parental, junctioned construct was 1.1 min^{-1} with a K_M of 0.032 μM, k_{cat} for the junctionless construct was 0.13 min^{-1}. Although the affinity of the substrate binding strand remained high in the junctionless complex (K_M apparent of 70 nM), the apparent interdomain K_M for loop B was 61 μM (*10*). The results of single-turnover kinetics suggested that the 10^4-fold reduction in catalytic efficiency was due mostly to an increase in the apparent K_M (*10*).

Over the past two decades since the discovery of the hairpin ribozyme, numerous functional groups have been identified including those that are essential for folding (*12*−*16*) and catalysis (*17*−*19*). Among these, G8 and A38 were shown to contribute directly in the chemical steps of the reaction (*17*, *20*, *21*). The spatial location of these residues was revealed when high-resolution crystal structures of the hairpin ribozyme were solved in the 4WJ form (*22*, *23*). This work suggested a possible acid/base catalysis mechanism (*17*, *22*, *24*) and emphasized an important role for the exocyclic

[†] This work was supported by NIH Grant GM63162 to J.E.W.

[‡] Protein Data Bank codes for the reported structures: U39, 2D2K; U39C, 1X9C; U39(C3), 2D2L, and high salt 64-mer, 1X9K.

* To whom correspondence should be addressed. Mailing address: Department of Biochemistry and Biophysics, University of Rochester School of Medicine and Dentistry, Box 712, Rochester, NY 14642. Phone: 585 273-4516. Fax: 585 275-6007. E-mail: Joseph_Wedekind@URMC.Rochester.edu.

[§] Present address: Rosalind Franklin School of Science and Medicine, Dept. of Biochemistry and Mol. Biol., 3333 Green Bay Road, N. Chicago, IL 60064.

[||] Present address: Brandeis University, Dept. of Biochemistry, Waltham, MA 02454.

[1] Abbreviations: 4WJ, four-way helical junction; C3, a three carbon propyl linker comprising atoms P, O1P, O2P, O5′, C5′, C4′, C3′, and O3′; W−C, Watson−Crick; C, cytidine; PEG 2K MME, poly(ethylene) glycol 2000 mono methyl ether; 2′-OMe, 2′-deoxy-2′-O-methyl; H-bond, hydrogen bond; rmsd, root-mean-square *XYZ* displacement; CMCT, 1-cyclohexyl-*N*′-[2-(*N*′-methylmorpholino)ethyl] carbodiimide-*p*-toluene sulfonate; NiCR, (2,12-dimethyl-3,7,11,17-tetraazabicyclo-[11.13.1]heptadeca-1(17),2,11,13,15-pentaenato)nickel(II) perchlorate.

10.1021/bi051550i CCC: $30.25
Published on Web 10/15/2005

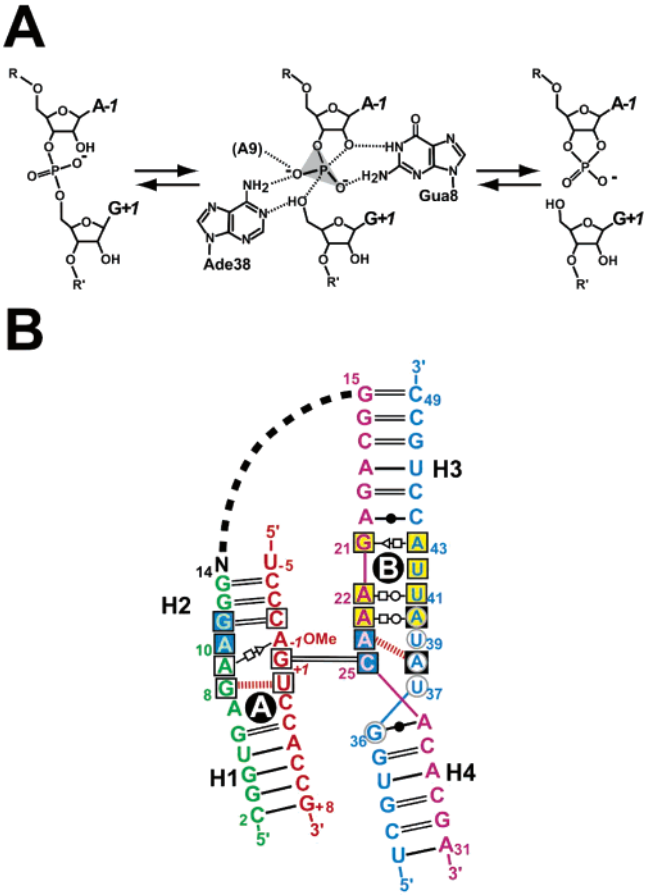

FIGURE 1: Schematic diagrams of the hairpin ribozyme reaction and secondary structure of the construct used in this study. (A) Bond cleavage proceeds through a trigonal bipyramidal transition state resulting in a cyclic-2′,3′-phosphodiester bond and a free 5′-OH group. The bases at G8 and A38 play essential roles in catalysis and transition state stabilization. (B) Secondary structure of the minimal hairpin ribozyme adapted from RNAview (*61*). Nucleotides of the substrate strand are depicted in red; other ribozyme strands are colored green, purple, or blue. This color scheme is preserved throughout the figures. H-bond pairings: open-square, Hoogsteen; open triangle, trans-sugar; open circle, W−C face; and closed circle, wobble pair. Double and single lines indicate W−C H-bond pairs; the dashed red line indicates a single H-bond. The loop A and B domains are labeled with conserved residues boxed; boxes with blue backgrounds indicate residues of the ribose zipper; yellow filled boxes indicate residues of the E-loop; gray circled positions belong to the S-turn. A 2′-OMe indicates an inert substitution at A−1. The dashed line between positions 14 and 15 represents the covalent bond observed in "junctioned" forms of the ribozyme. Position 14 was omitted in this study.

amines of A9, G8, and A38 in transition-state stabilization (*25*). More recent proposals feature electronic stabilization of the oxyphosphorane intermediate based on exogenous nucleobase rescue (*18*, *21*, *26*).

To provide insight into the relationship between hairpin ribozyme structure and function, we asked the question of how "gain-of-function" mutations influence the RNA structure. The U39C alteration was of special interest because it was identified in selection experiments designed to elucidate the minimal catalytic core (*27*, *28*) and alter substrate specificity (*29*). By itself, U39C served as an activator of the wild-type ribozyme that increased k_{cat} by 4-fold relative to the native ribozyme (*29*). Interestingly, its rate-enhancing properties worked optimally at relatively low Mg^{2+} levels ($\leq$3 mM) (*28*, *29*) suggesting a mechanism in which metals could compensate for the structural effects of the U39C substitution (*29*). In contrast, the mutation of U39 to a propyl linker (C3) appeared relatively insensitive to Mg^{2+} concentrations (*30*, *31*), suggesting an uncoupling from the effects of metal binding. This mutant also exhibited a gain-of-function effect with an approximately 3-fold increase in k_{cat} over the native ribozyme (*30*, *31*).

To elucidate the structural basis for the various U39 gain-of-function mutations, we undertook a structural investigation of the hairpin ribozyme in a form amenable to site-directed mutagenesis and single-atom modifications (Figure 1B). To best document the effects of the various mutations, we solved three nearly isomorphous crystal structures representing (i) the native ribozyme (U39); (ii) the U39C mutant, and (iii) the U39(C3) mutant. The results revealed that the native ribozyme structure adopts two nucleotide conformations at position U37 that can be considered "sequestered" and "exposed" forms. Structures of U39C and U39(C3) exhibited only the sequestered conformation of U37, which packs against G+1 at the active site. All three structures displayed a $Co(NH_3)_6^{3+}$ ion bound in the major groove at the confluence of the E-loop and S-turn. These results are discussed in the context of the S-turn structure, gain-of-function activity, and metal dependence of the respective mutants.

EXPERIMENTAL PROCEDURES

Development of Minimal Hairpin Ribozyme Crystallization Constructs. The design and use of a minimal, junctionless hairpin ribozyme construct for structural studies was inspired by studies of the Burke lab (*10*). Initial crystallization efforts involved a variety of constructs with the best crystals comprising an all-RNA, blunt-ended 64-mer that grew from solutions of 1.8 M $(NH_4)_2SO_4$ (*32*) and diffracted X-rays to 3.17 Å resolution (Table 1). This construct of the hairpin ribozyme was solved by molecular replacement (see below), and its structure was used to rationally engineer the 61-mer of this study (Figure 1B), resulting in crystals with superior diffraction properties (Table 1).

Crystallization and X-ray Diffraction Analysis. RNA strands for the loop A and B domains, and mutants thereof, were obtained from Dharmacon Inc. Sequences of the four strands of the 61-mer are depicted in Figure 1B. Position U39 was replaced by either C or C3 as necessary. Strands were purified and docked to form the minimal hairpin ribozyme in the presence of 0.5 to 1.5 mM $Co(NH_3)_6Cl_3$ as described (*32*). $Co(NH_3)_6Cl_3$ was chosen because it elicited a more robust docking interaction than Mg^{2+}, requiring 50-fold lower concentrations (*33*). Diffraction quality crystals of the redesigned 61-mer were identified in hanging-drop vapor diffusion experiments that tested several grid screens empirically formulated for RNA (*32*, *34*). Crystals of the native and U39C hairpin ribozyme 61-mer were obtained from solutions of 22−24% (w/v) PEG 2K MME, 0.25 M Li_2SO_4, 0.10 M Na-cacodylate pH 6.0, 2 mM spermidine-HCl, and 2.5 mM $Co(NH_3)_6Cl_3$. The best crystals of the U39-(C3) mutant grew from 25.5 to 26.5% PEG 2K MME, 0.25 M Li_2SO_4, 0.1 M Na-HEPES pH 7.6, 2 mM spermidine-HCl, and 1.25 mM $Co(NH_3)_6Cl_3$. Crystals of the native and U39(C3) hairpin ribozymes grew as hexagonal rods at 20 °C and reached a maximum size of 100 μm × 140 μm ×

Table 1: X-ray Diffraction and Refinement Statistics

	high salt (U39C) 64-mer	U39 (native) 61-mer	U39C 61-mer	U39(C3) 61-mer
cell dimensions (Å)	$a = 94.1$, $c = 128.6$	$a = 93.2$, $c = 126.4$	$a = 93.3$, $c = 128.0$	$a = 93.2$, $c = 122.2$
resolution (Å)	3.17 to 24.6	2.65 to 34.0	2.19 to 25	2.50 to 30.7
total reflections	46 944	115 565	171 048	146 295
unique reflections	6085	9889	17 084	11 302
redundancy	6.6 (7.0)	11.7 (12.1)	8.0 (5.6)	12.9 (13.1)
completeness (%)[a]	98.3 (100)	99.5 (100)	98.3 (97.9)	99.0 (99.3)
$\langle I/\sigma(I)\rangle$[a]	13.4 (3.9)	24.0 (7.4)	26.7 (4.5)	29.6 (7.0)
R_{sym} (%)[a,b]	6.4 (41.2)	7.0 (36.3)	3.6 (37.1)	5.1 (42.0)
no. of RNA atoms	1313	1374[e]	1312	1300
no. of waters	none	9	42	8
no. of ions	none	2 $Co(NH_3)_6$(III), 1 SO_4^{2-}	2 $Co(NH_3)_6$(III), 1 SO_4^{2-}	3 $Co(NH_3)_6$(III), 1 SO_4^{2-}
RNA/$Co(NH_3)_6^{3+}$ av *B*-factors (Å^2)	160.9/na	55.0/69.0	59.7/63.8	60.6/58.8
R_{cryst}/R_{free} (%)[c,d]	23.6/25.2	24.7/27.0	24.9/26.3	22.6/24.9
rmsd bonds (Å)	0.009	0.007	0.006	0.007
rmsd angles (deg)	1.60	1.50	1.40	1.40

[a] Highest resolution shell statistics are noted parenthetically: 3.17−3.28 Å; 2.65−2.74 Å; 2.19−2.33 Å, 2.50−2.59 Å. [b] $R_{sym} = \sum|I_j - \langle I_j\rangle|/\sum|I_j| \times 100$. [c] $R_{cryst} = \sum_{hkl}|F_o - kF_c|/\sum_{hkl}|F_o| \times 100$, where k is a scale factor. [d] R_{free} is defined as the R_{cryst} calculated using 8−10% of the data selected randomly and excluded from refinement. [e] The number of atoms reported includes dual conformations for U37, A38, and U39.

300 μm over 3 weeks. Crystals of the U39C mutant grew as hexagonal prisms that reached a maximum size of 250 μm × 250 μm × 350 μm in 1 month.

X-ray Diffraction Experiments. All crystals were harvested and cryoprotected by 3 min transfers into synthetic mother liquors comprising the contents of well solutions fortified with successively higher amounts of glycerol ranging from 5% to 17.5% (v/v). At these levels of PEG and glycerol, $Co(NH_3)_6Cl_3$ solubility was limited to approximately 0.5 mM. Single crystals were captured by surface tension in 20 μm thick rayon loops (Hampton Research) and flash cooled to −190 °C by exposure to a cold nitrogen gas jet generated by an X-stream (Rigaku/MSC). Crystals were screened in-house for X-ray diffraction on an R-AXIS IV image plate system at a crystal-to-detector distance of 15 cm; X-rays were generated by an RU-H2R rotating anode generator (Rigaku/MSC) operated at 5 kW and equipped with a 0.3 mm focal cup. X-rays were monochromated and focused by use of confocal optics (Rigaku/MSC). Complete data sets were recorded for the native and U39(C3) samples and used for refinement (Table 1). Each data set comprised ∼200 images of width 0.5° and utilized an exposure time of 50 min per degree. The U39C and high salt 64-mer crystals were removed from the in-house goniometer head by use of 18 mm cryotongs (Hampton Research) and stored in liquid nitrogen. X-ray diffraction data for the high salt 64-mer (*32*) were collected at the Advanced Photon Source (APS) beamline ID-22, operated by the Southeast Regional Collaborative Access Team (SER-CAT). Data were recorded in two passes on a MAR165 CCD detector (Mar Research) at crystal-to-detector distances of 22 and 27 cm. A total of 140 images were collected in the high-resolution pass as 0.5° rotations per image with an exposure time of 40 s per degree; 40 low resolution images were recorded as 2° rotations per image with an exposure time of 1 s per degree. X-ray data for the U39C mutant were recorded at beamline A1 of the Cornell High Energy Synchrotron Source (CHESS) on a Quantum210 CCD detector (ADSC) at a crystal-to-detector distance of 22.5 cm. Data were recorded as 190 images with a rotation angle of 0.5° per image with an exposure time of 80 s per degree. All data were reduced using the CrystalClear software package (*35*). Intensity and data reduction statistics are reported in Table 1.

Structure Determination, Refinement, and Analysis. The structure of the high salt hairpin ribozyme 64-mer was solved by molecular replacement using AMoRe (*36*) and contained one hairpin ribozyme molecule per asymmetric unit. The search model was derived from the core structure of the 4WJ−U1A complex (PDB entry 1HP6). The structure was refined in CNS (*37*) using rigid body refinement, simulated annealing, positional minimization, and individual *B*-factor refinement; manual adjustments were performed using the interactive graphics program *O* (*38*). The low salt 61-mers were solved by rigid body refinement of the entire structure, as well as the individual loop A and B domains, followed by conventional refinement methods as described for the 64-mer. Assignment of waters in the 61-mers was based upon H-bond distances and geometry of donor and acceptor groups. The possibility that ions were present in lieu of water was unlikely because the crystallization medium comprised 0.5 M Li^+ and 0.1−0.3 mM $Co(NH_3)_6Cl_3$, which is relatively inert to ligand exchange compared to Mg^{2+}(aq). Temperature factors of refined waters matched those of neighboring RNA atoms. All structures exhibited an alternate conformation for position U−5, which engages in a (designed) dyad-related crystal packing interaction that formed a U·U pair. A dual conformation was also modeled for positions U37−U39 in the native structure (Figure 2A and Table 1). The occupancies of these atoms were set empirically to 0.5, which optimized the agreement between individual atomic B-factors of each conformation; these refined conformations were shown to be featureless in σA-weighted ($mF_o - DF_c$) electron density maps. Two $Co(NH_3)_6^{3+}$ ions were observed consistently in all 61-mer structures. Assignment of these ions was based on their octahedral coordination geometry to amine ligands and ≥8σ anomalous difference Fourier peaks observed in electron density maps calculated from data sets recorded at $\lambda = 1.54$ Å. A third $Co(NH_3)_6^{3+}$ ion was observed in the U39(C3) structure, although this site has low occupancy. Superpositions were performed for all matching atoms using LSQKAB (*39*). Superpositions with the 4WJ hairpin ribozyme were performed using chains A−C of PDB entry

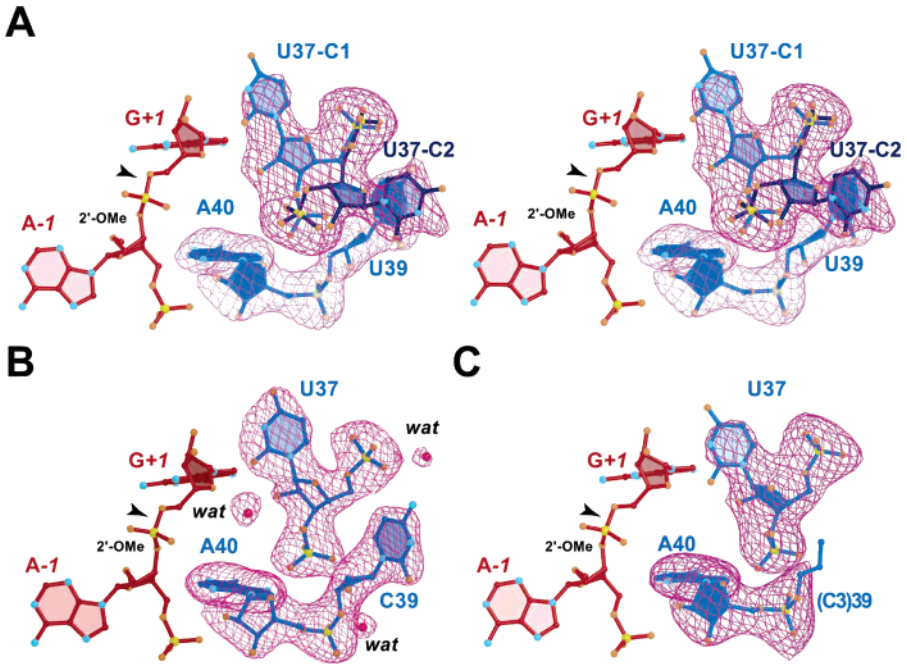

FIGURE 2: Representative simulated annealing omit electron density maps for the S-turn (residues U37 to 40) of the minimal, all-RNA hairpin ribozymes. Nucleotides are depicted as ball-and-stick models with residues labeled; the scissile bond is marked with an arrowhead. Maps are contoured at the 4σ level and have coefficients (mF_o − DF_c). (A) Stereo diagram of the native, U39, hairpin ribozyme revealing alternate conformations for residue U37. Conformers are labeled C1 (sequestered) and C2 (exposed). C1 is depicted in light blue, whereas C2 is dark blue. The map was calculated using data between 2.65 and 34 Å resolution. The dual conformations modeled for A38 and U39 were omitted for clarity. (B) Mono depiction of electron density for the U39C mutant calculated using data between 2.19 and 25 Å resolution. Solvent molecules are labeled "wat". (C) Mono depiction of electron density for the U39(C) mutant calculated using data between 2.50 and 31 Å resolution. The site of the propyl linker is labeled (C3)39.

1M5K. Buried surface areas were calculated using CNS (*37*). Statistics for the refined structures are reported in Table 1. Figures 2 through 5 and 6C were made by use of Bobscript (*40*). Figures 6A and 6B were produced with Pymol (*41*).

RESULTS

Structure Determination, Construct Design, and Model Quality. The RNA sequence of the high salt crystal form of the minimal, all-RNA 64-mer hairpin ribozyme, described previously (*32*), was derived from the negative polarity RNA strand of satellite tobacco ringspot virus. The crystal structure of this hairpin ribozyme was solved by molecular replacement to 3.5 Å resolution using the core nucleotide coordinates of the 4WJ−U1A hairpin ribozyme complex (*22*). Molecular replacement was complicated because correct solutions exhibited R_{cryst} values of nearly 54%. However, solutions were pursued when correlation coefficients exceeded 0.6 and demonstrated reasonable crystal packing. Refinement of the high salt crystal form to 3.17 Å resolution (Table 1) revealed that three nucleotides of loop A were disordered at the duplex ends. To improve X-ray diffraction, a new crystallization construct was developed (Figure 1B) that included (i) substitution of A−U rich pairs in H1 with three tandem G−C pairs to prevent fraying of the duplex end; (ii) use of a 5′-U overhang in H2 to promote dyad symmetric packing; and (iii) shortening of H1 by 1 base pair. This 61-mer variant of the minimal, junctionless all-RNA hairpin ribozyme also crystallized in space group $P6_122$, but under low salt conditions. Because the unit cell dimensions of the 61-mer and its mutants are comparable to those of the high salt 64-mer (Table 1), their structures could be solved by difference Fourier methods. The quality of these structures is indicated by their reasonable R_{cryst} values, and R_{free} values within 3% of R_{cryst} (Table 1). These values are comparable to those of other small ribozyme structures (*42*−*44*). Representative simulated annealing omit electron density for the S-turns of all three structures indicated well-defined sugar puckers and base conformations, especially for the U39C structure at 2.2 Å resolution (Figure 2). The native U39 structure was of sufficient quality to model a dual conformation for position U37 (Figure 2A). To varying degrees, each structure revealed solvent molecules that mediated contacts between RNA functional groups (Figure 2B). Electron density maps of all structures were contiguous, and no disorder was observed except for a break at the propyl linker of the U39(C3) structure (Figure 2C), where electron density could only be seen at lower contour levels. The quality of the low salt crystal forms was indicated further by their lower average temperature factors of 58.5 Å^2 compared to 160.9 Å^2 for the high salt form (Table 1).

Fold of the Minimal Hairpin Ribozyme. The overall structure of the minimal hairpin ribozyme revealed a Y-shaped molecule when viewed from its broadest face (Figure 3A). The longest dimension was the loop B domain helix−loop−helix, which spans 60 Å from A31 to C49. The length of the loop A domain is 30 Å from U−5 to C2, and its principal axis is oriented nearly perpendicularly to the loop B axis. The horizontal width of the complex, as viewed in Figure 3A, is 31 Å when measured from the backbone of G8 to that of A22. The tertiary interface between the two helix−loop−helix domains forms a sequestered active site at the confluence of A−1, G+1, G8, and A38. The internal loop of the A domain harbors the cleavage site, which is distorted about the scissile bond such that the N-glycosidic

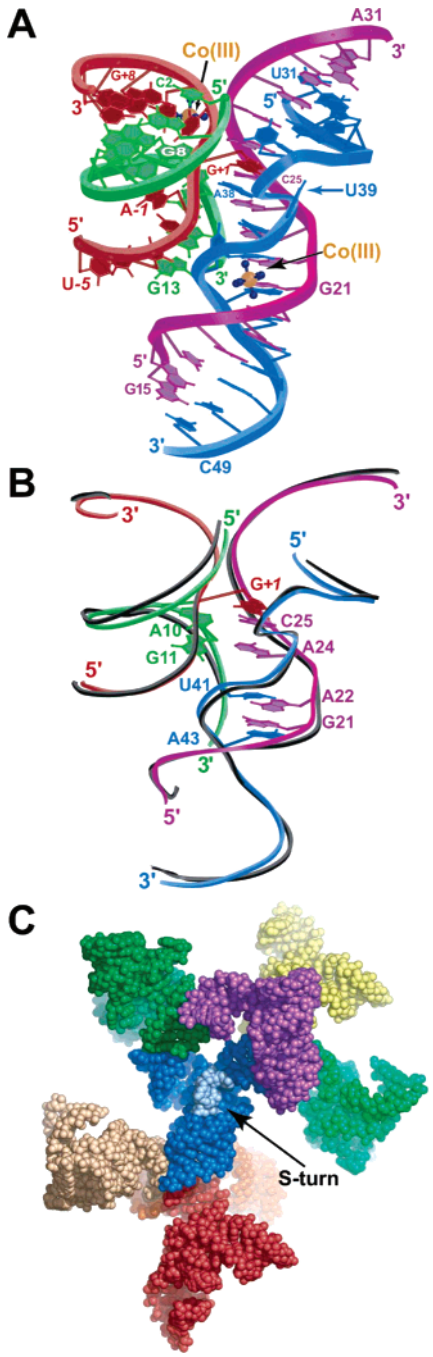

FIGURE 3: Schematic ribbon diagrams and crystal packing interactions for the minimal, all-RNA hairpin ribozyme. (A) Representative ribbon diagram of the U39C mutant comprising atoms of the phosphate backbone to depict the overall tertiary fold. Nucleotides are drawn as ball-and-stick models with ribose omitted for clarity. The $Co(NH_3)_6^{3+}$ binding sites (orange and blue, ball-and-stick models) are identified as Co(III). Key nucleotides are labeled as in Figure 1B. (B) A ribbon diagram of the minimal, native U39 hairpin ribozyme, colored as in (A), superposed with the corresponding nucleotides of the 4WJ−U1A complex (black), reported previously (PDB entry 1M5K). Nucleotides of the various conserved structural motifs are drawn as ball-and-stick models including E-loop residues G21, A22, U41, and A43; the ribose zipper, residues A10, G11, A24, C25; and the interdomain W−C pair, G+1 and C25. (C) Space-filling model of the crystal packing observed for the minimal hairpin ribozyme lattice. Each molecule of the unit cell is depicted in a distinct color to emphasize the end-to-end helix packing. The central structure (blue asymmetric unit) possesses a labeled S-turn (light blue). This region is devoid of crystal contacts. For perspective, the purple molecule points forward, whereas the orange and yellow molecules point backward.

linkages of A−1 and G+1 exhibit a nearly 90° twist (Figures 2A and 3A). The minimal hairpin ribozyme adopts nearly in-line phosphoryl transfer geometry (Figure 1A), which comprises the angle between the 2′-oxygen of A−1, the electrophilic phosphorus of G+1, and the O5′-leaving group (Figure 2A); a 2′-OMe was used at position A−1 to prevent cleavage (Figures 1A and 2A). The 2′-OMe modification appears to distort the local sugar pucker into a C2′-endo conformation whereas a previously described 4WJ−U1A−vanadate complex, an approximate mimic of the transition state, exhibited a distinctly C2′-exo conformation at A−1 (*23*). The geometry of the active site and scissile bond of the minimal hairpin ribozyme are remarkably similar to those of a 4WJ hairpin ribozyme crystal structure also solved in the presence of a 2′-OMe at position A−1 (*22*).

Minimal versus Four-Way-Junction Hairpin Ribozyme Folds. To compare the overall fold of the minimal, native hairpin ribozyme with that of the 4WJ structure reported previously (*22*), a superposition was performed (Figure 3B). The core nucleotides remained nearly unaltered with an average rmsd of 1.28 Å, despite 54% differences in sequence over 61-nucleotides. The largest discrepancies, excluding the S-turn region (see below), occurred at the ends of the helical stems within the substrate (red) and ribozyme (purple) strands (Figure 3B), exhibiting an average rmsd of 2.48 Å. These differences occurred most likely as a result of crystal packing at the exposed hydrophobic ends of the minimal hairpin ribozyme duplex (Figure 3C). In contrast, the rmsd for all atoms comprising the scissile bond at A−1 and G+1 was 0.67 Å indicating that atoms in the core of each independently determined structure showed excellent spatial agreement. Docking of the loop A and B domains of the minimal junctionless hairpin ribozyme buried 1150 Å^2, which concurs with the measured interdomain $K_M^{\text{loop B}}$ of 0.4 μM (*33*), if one considers buried surface area as an indicator of thermodynamic stability (*45*). This area is comparable to that of the 4WJ hairpin ribozyme, which sequesters 1570 Å^2 for the entire 113 nucleotide, multijunction complex (*22*). Collectively, these observations indicate that the minimal hairpin ribozyme is not significantly different from the fold of the 4WJ ribozyme, thus establishing it as a small, easily accessible synthetic construct for structure/function studies.

Other RNA structural motifs within the hairpin ribozyme (*22*) are preserved as well, based on comparisons of the minimal and 4WJ structures. These include the E-loop (*46*), which comprises a sheared G21·A43 base pair flanked by tandem Hoogsteen/W−C interactions at A22·U41 and A23·A40 (Figures 1B and 3B). Additionally, the unique interdomain G+1 to C25 W−C interaction is maintained (Figures 1B and 3B), as well as a "canonical" ribose zipper (*47*) involving H-bonds between the 2′-OH and N3 base atoms of A10, G11, A24, and C25 (Figure 3B); details for these interactions have been described elsewhere (*22*). The observation of a conserved ribose zipper is significant because previous studies reported differences in the folding energetics between minimal and 4WJ hairpin ribozymes (*48*). Specifically, no significant fold destabilization was observed for 2′-OH mutants of the 4WJ ribose zipper, suggesting that these groups did not stabilize the docked structure as they did in the minimal hairpin ribozyme. The crystallographic observations prove that both hairpin ribozyme structures retain an identical ribose zipper configuration and exemplify the

principle that two different ribozyme constructs can adopt the same global architecture despite contextual differences in the initial domains.

Influence of Protein on RNA in the Crystal Lattice. When considering the structure determinations of the 4WJ (*22*, *23*) and minimal, junctionless 61-mer of this study, the hairpin ribozyme represents the first example of a small ribozyme to be solved in the presence and absence of U1A. The latter splicing protein has been adopted by the RNA crystallographic community as a "first choice" crystal packing module, although no reports of structural control studies exist. As such, the results presented here provide a unique opportunity to evaluate how protein packing interactions can influence the local RNA fold in the context of the crystal lattice. An analysis of the minimal, all-RNA hairpin ribozyme indicated that crystal contacts occurred mostly through hydrophobic base stacking at the helical ends (Figure 3C) where 3034 Å^2 is sequestered from solvent. No crystal contacts were observed within the core of the minimal ribozyme, including the S-turn, and these regions are exposed to bulk solvent. In contrast, the 4WJ−U1A lattice exhibited crystal contacts throughout most of the structure with 4900 Å^2 buried per complex, in which 37% of these packing interactions are attributable to U1A. Although a pairwise superposition between the minimal and 4WJ hairpin ribozymes indicated high levels of agreement, significant differences were observed in the S-turn, where alternate conformations of U37 (Figure 2A) differed by maximum rmsd values of 12.6 Å and 5.4 Å, corresponding to the C1 and C2 conformations (Figure 4A), respectively. The solvent exposed U37-C2 conformer was consistent with that previously reported for the 4WJ−U1A complex, although U37 adopted a single conformation in the asymmetric unit of the 4WJ−U1A structures and appeared to point toward bulk solvent (*22*, *23*).

However, a thorough analysis of the 4WJ−U1A crystal lattice revealed a significant interaction between the S-turn and a U1A molecule from a symmetry-related complex. Specifically, atom O4 of U39 in the 4WJ−U1A complexes (*22*, *23*) forms two H-bonds of ∼2.5 Å and 3.1 Å with atoms NH1 and NH2 of the guanidinium moiety of Arg70′ (Figure 4A). A second H-bond from Arg70′ contacts a nonbridging oxygen atom of the U37 phosphate backbone. Furthermore, the base of U37 is within 3.6 Å of the Arg70′ guanidinium group, consistent with a π-stacking interaction (Figure 4A). These conformational restraints arising from U1A appear to propagate to the furanose ring at position A40, which exhibits a distinctly different structural conformation compared to the minimal hairpin ribozyme of this study (Figure 4A). Nonetheless, the overall close spatial agreement between the U37-C2 conformations of both minimal and 4WJ hairpin ribozyme crystal structures (Figure 4A) suggested that the U1A contacts simply stabilized one of two conformers normally present in solution. The interconversion of these conformers appears readily accessible through rotations in the phosphate backbone at positions 37 and 38 (Figures 2A and 4A).

Structural Differences in the S-Turn Resulting from the U39C and C3 Propyl Linker Modifications. To explore structural differences elicited by the U39C and U39(C3) mutants, their respective structures were superimposed on the minimal, native hairpin ribozyme (Figures 4B and 4C) resulting in rmsd values of 0.36 and 0.37 Å. Interestingly, both mutations appeared to shift the equilibrium conformation of U37 toward the sequestered (C1) state that packs against G+1 (Figures 2B and 2C and Figures 4B and 4C). Changes from C2 to C1 were associated with altered H-bonds in the S-turn (Figures 4E and 4F). For mutant U39C, substitution of the O4 keto oxygen at U39 with an exocyclic amine resulted in a new ∼3.0 Å H-bond to the pro-*R* phosphate oxygen of U37 (Figures 4B and 4G). This interaction was not present in either the native or U39(C3) structures due to the absence of a suitable H-bond donor at substituent 4 of the pyrimidine ring (Figures 4C, 4E, 4F, and 4H). The structure of the U39C mutant was accompanied also by formation of a new ∼2.6 Å H-bond between the C39 2′-OH and the A38 pro-*R* phosphate oxygen (Figures 4B and 4G). At 2.6 Å resolution, the sugar pucker of the native hairpin ribozyme was discernible at U39 (Figure 2A). Hence, it is possible that the 2′-OH of U39 forms an equivalent H-bond with the pro-*R* phosphate oxygen at A38 in the U37-C1 structure (Figure 4F), albeit the distance between these functional groups is 3.5 Å, making such an interaction weak. Due to the dual conformation of this residue, such an H-bond would be present only half the time due to differences in the U39 sugar puckers (Figures 4B and 4E versus 4F). Hence, a net H-bond difference of 0.5 exists between the native and U39C hairpin ribozymes at this position. Notably, the latter A38 phosphate to 2′-OH interaction was absent in the U39(C3) mutant, because it is missing the requisite 2′-hydroxyl group (Figures 4C and 4H).

The largest conformational change observed in the native versus mutant structures was at position U37 of the S-turn (residues G36 through A40). This difference constituted a 13 Å change in the location of the uracil base, which abuts the ribose of G+1 in both the U39C and U39(C3) mutants (Figures 4B and 4C and 4G and 4H). No conformational heterogeneity is observed in either mutant at this position, unlike the native structure. For the U39C mutant, the 2′-OH of U37 forms an ∼2.6 Å H-bond to an ordered solvent molecule that mediates a 2.7 Å contact to O4′ of G+1 (Figures 2B, 4B and 4G). Equivalent solvent molecules did not appear in the electron density maps of native and U39-(C3) mutants, most likely due to their lower resolution (Table 1), as well as the conformational heterogeneity of the native structure. Notably, the W−C face of U37 does not engage in direct H-bond interactions with G+1 in any of the minimal hairpin ribozyme structures. Distances are limited to ≥3.8 Å (Figure 4C). Similarly, the distance between the 2′-oxygen of U37 and O4′ of G+1 is 3.6 Å, thereby precluding a direct H-bond contact.

In a final structural comparison, mutants U39C and U39-(C3) were superimposed resulting in an rmsd of 0.42 Å. Based on this analysis one additional H-bond was assigned to the mutants that was not observed in the native structure. Specifically, the pro-*S* oxygen equivalent at position 39 forms an ∼2.7 Å H-bond with the 2′-OH group of G36 (Figures 4D, 4G and 4H). The absence of this interaction in the native structure appears to be the result of a change in the sugar pucker at G36. Hence, the total number of RNA-to-RNA H-bonds gained in the U39C structure was three (compare Figures 4E and 4F to 4G), whereas the U39(C3) structure exhibited one, relative to the native hairpin ribozyme (compare Figures 4E and 4F to 4H). Other aspects of the U39(C3) mutant included a prominent ∼1 Å shift of its A38

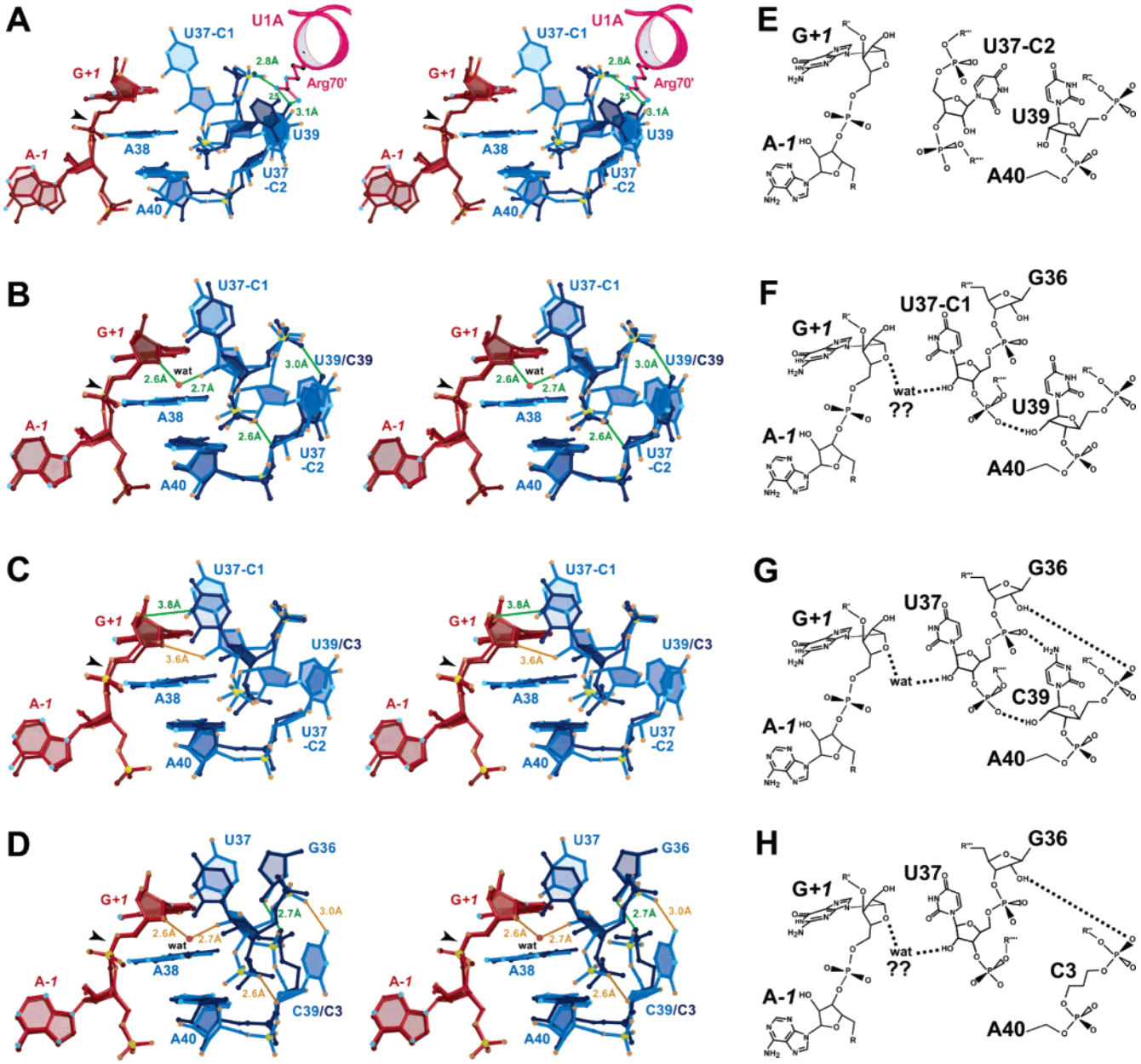

FIGURE 4: Stereographic ball-and-stick diagrams of S-turns depicting superpositions of various native and mutant hairpin ribozyme crystal structures and schematic drawings of the respective U37 H-bond environments. Green and orange lines in parts A to D show possible H-bonds or associated distances for a given structure. (A) Comparison of the native minimal hairpin ribozyme structure (red and light blue) to the 4WJ structure (brown and dark blue). A helix from a crystallographically related U1A protein molecule is shown (pink). The dual C1 and C2 conformations for U37 are labeled as in Figure 2A. The ribose of A38 was omitted for clarity. (B) Comparison of the native minimal hairpin ribozyme structure (red and light blue) to the U39C mutant structure (brown and dark blue). The red sphere labeled "wat" indicates a solvent molecule. (C) Comparison of the native minimal hairpin ribozyme structure (red and light blue) to the U39(C3) mutant structure (brown and dark blue). (D) Comparison of the U39C mutant of the minimal hairpin ribozyme structure (red and light blue) to the U39(C3) mutant structure (brown and dark blue). The ribose of G36 has been added to illustrate the potential for formation of a new H-bond. (E) The environment of U37-C2 in the context of the native, U39 structure. (F) The environment of U37-C1 in the context of the native, U39 structure. Possible H-bonds are indicated as dashed lines. The interaction with water is inferred from the high-resolution U39C structure in (B). (G) The environment of U37 in the context of the U39C mutant. (H) The environment of U37 in the context of the mutant U39(C3) structure. The interaction with water is inferred from the high-resolution U39C structure in (B).

phosphate backbone into a pocket created by removal of the U39 base (Figure 4D). Consequently, the U37 base of U39-(C3) pivoted relative to the native and U39C structures such that its N3 position is within 3.8 Å of G+1 O3′ (Figures 4C and 4D). Remarkably, the replacement of U39 with a propyl linker caused no major structural changes in the S-turn. This is consistent with previous functional studies in which mutations of U to any other base were tolerated (*49*, *50*). Likewise chemical modification studies suggested that U39 exhibited a highly exposed structure (*51*) leading to the conclusion that this position serves primarily as a spatial linker (*12*, *30*, *49*). However, unlike the U39C gain-of-function mutation, replacement of U39 with a propyl linker resulted in a highly metal *insensitive* activity over a wide concentration range of Mg^{2+} (*30*).

Cobalt Hexaamine Binding. $Co(NH_3)_6^{3+}$ was chosen for structural studies of the minimal, junctionless hairpin ribozyme because prior solution studies demonstrated that it

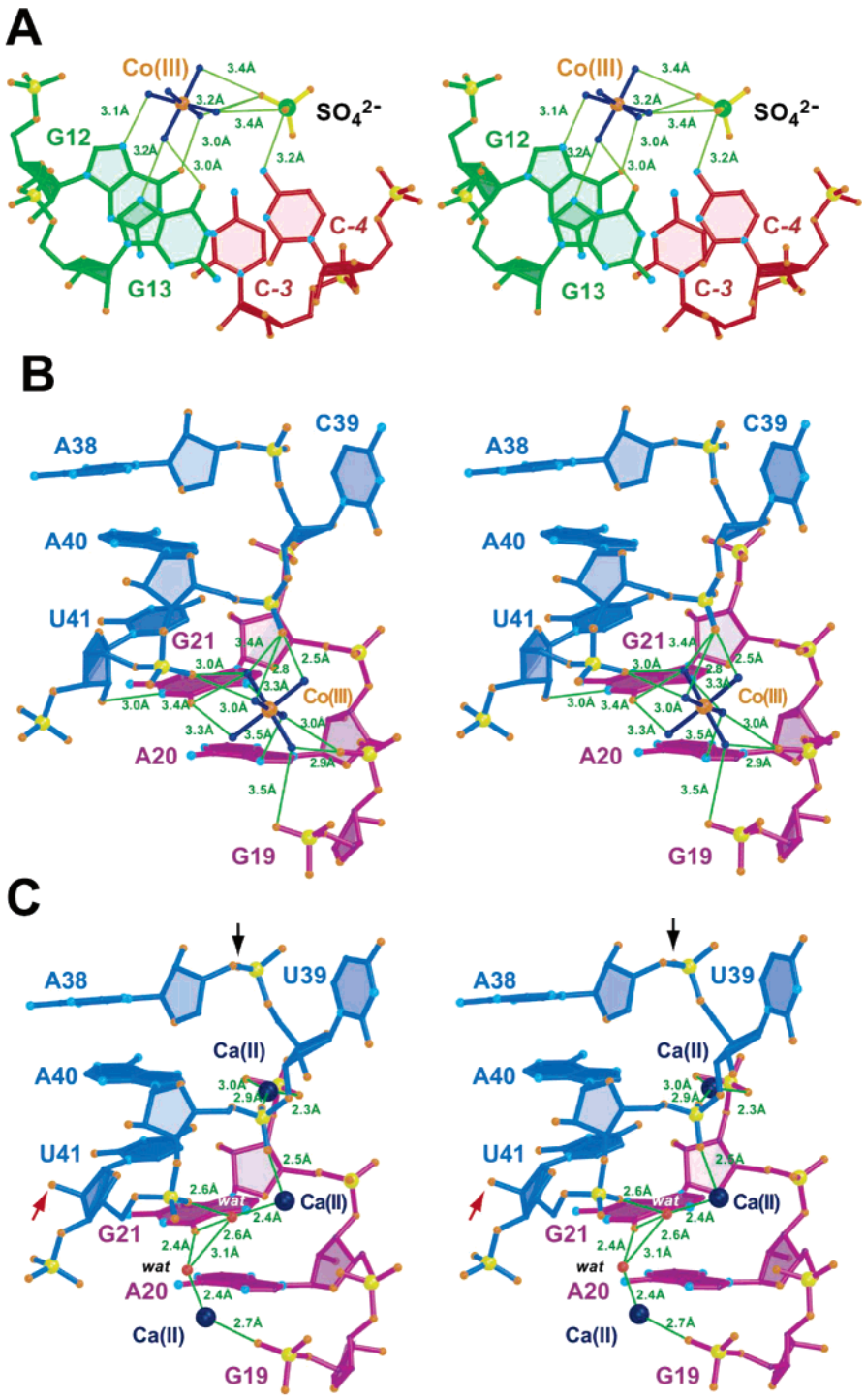

FIGURE 5: Stereographic ball-and-stick diagrams depicting multivalent ion binding sites in the hairpin ribozyme. (A) Representative metal binding site I of the minimal hairpin ribozyme. Cobalt hexaamine [Co(III)] is depicted as a ball-and-stick model with orange cobalt and dark blue amine ligands. Metal−amine distances are ~2.0 Å; coordination distances are provided; a sulfate ion is depicted as a ball-and-stick model labeled SO_4^{2-}. (B) Representative metal binding site II of the minimal hairpin ribozyme depicted as in (A). The binding site represents the interface of the E-loop (A20 and G21) with the S-turn (A38 through A40). (C) Representative metal binding site II (equivalent) for the 4WJ hairpin ribozyme structure (PDB entry 1M5K). Calcium ions are depicted as spheres (blue) with bound waters (red). The red and black arrows depict regions that differ from the conformation of the minimal hairpin ribozyme structure in (B).

stimulated a stronger interaction between the loop A and B domains compared to Mg^{2+} (*33*). Unlike other small ribozymes, the hairpin ribozyme does not require inner sphere metal ion coordination for catalytic activity as demonstrated by its ability to function in the presence of $Co(NH_3)_6^{3+}$ (*52*, *53*); appropriately, cobalt hexaamine is a structural mimic of hydrated Mg^{2+} that is relatively inert to ligand exchange (*54*). Two major cobalt hexaamine ion binding sites were observed in all three minimal hairpin ribozyme structures (Figure 5A and 5B, Table 1). The first position (site I) bound in H2 of the loop A domain (Figures 3A and 5A). Here the hexaamine ligands make specific major-groove contacts to the duplex by binding to the N7 and O6 atoms of tandem guanine nucleotides located at positions 12 and 13 (Figure 5A). The amine ligands also interact with a sulfate ion that engages in H-bonds to the exocyclic amine of C−4 (Figure

5A). This observation helps explain the strong preference for sulfate anions in crystallization. Notably, site I resides near a crystallographic 2-fold axis comprising the engineered U·U pair at A−5 (Figure 1A) where cobalt and sulfate mediate a crystal contact. The mode of $Co(NH_3)_6^{3+}$ binding at site I is reminiscent of cobalt hexaamine interactions with tandem purine bases in the major groove of $tRNA^{Phe}$ (*55*).

A second $Co(NH_3)_6^{3+}$ coordination (site II) was observed in the major groove of the E-loop motif in the B domain (Figures 1B and 3B). Unlike site I, each of the hexaamine ligands engages in multiple coordination interactions with neighboring nucleotide bases, as well as nonbridging oxygen atoms of the RNA backbone (Figure 5B). Specific base contacts occur at both O6 and N7 atoms of G21 (Figure 5B). Robust binding with the phosphate backbone also occurs at positions 20, 40, and 41. The interactions at position 40 are extensive and exhibit a nearly tetrahedral H-bonding pattern that agrees with the electronic distribution of the nonbridging oxygen (Figure 5B). Site II also corresponds to the location of two Ca^{2+} ions that were observed in 4WJ hairpin ribozyme crystal structures (Figures 5B and 5C). In each independent structure, the ions appear to fulfill the role of stabilizing the structural transition between the E-loop and the S-turn, which places a significant amount of opposing negative charges into the major groove.

Changes in the E-Loop/S-Turn Transition. Differences exist between the minimal hairpin ribozyme and 4WJ structures at the transition between the E-loop and S-turn. Most notably, the 2′-OH of ribose at U41 of the minimal ribozyme engages in a ∼3.0 Å H-bond with the imino group of G21. This interaction is absent in the 4WJ structures (Figure 5B versus 5C). Evidence that this interaction occurs in solution is based upon nucleotide analogue interference mapping experiments that showed that 2′-deoxy-2′-fluoro U41 interfered with hairpin ribozyme activity, although the interference from 2′-deoxy U41 was moderate (*15*). Hence, whereas the 4WJ structure would readily accommodate either modification (Figure 5C, red arrow), the minimal ribozyme structures suggest that this modification would result in more than the loss of a single H-bond. The associated reduction in ribozyme activity would be due to the proximity of the essential residue A38, which base stacks on this motif, succumbing to the preference of the 2′-deoxy-2′-fluoro adduct to adopt a C3′-endo furanose conformation (*56*). Interestingly, the sugar puckers at A38 also differ between the minimal and 4WJ structures (Figure 5B versus 5C, black arrow). The significance of this deviation (if any) is unknown, but may be indicative of rearrangements induced by differential metal binding in this region or as a result of variations in the local crystallographic environment.

U37 Affects Accessible Surface Area at the Active Site. A search for binding interactions responsible for the U39C or U39(C3) gain-of-function, as well as the absence of direct H-bond contacts between G+1 and U37, prompted an analysis of solvent accessible area associated with the U37-C2 to C1 transition in the native hairpin ribozyme (Figures 6A and 6B). Differences in buried surface area occurred at positions of the S-turn encompassing residues 36 to 39, with the exception of A38 whose accessible area remained nearly constant. Nucleotides G+1 and U+2 of the loop A domain also became more sequestered, but not A−1. Treating both conformations of U37 as discrete (i.e. fully occupied) populations, a net difference in area of 120 $Å^2$ was calculated, indicating an increase in buried surface area of conformation U37-C1 relative to U37-C2. The greatest changes occurred at G36 and U37 in which the minor groove edge of the G36 base packed edge-on against the base of U37 in the sequestered conformation (Figure 6B). Comparable changes in buried area were observed as well for the U39C and U39-(C3) mutations relative to the exposed, U37-C2 conformation of the native structure (Figure 6A versus 6B). Notably, only modest contacts were observed between the base of U39 and the ribose of U37 in conformation C2 (Figure 4B). Overall, the solvent accessibility of the U39 base and the exposed U37-C2 conformation are expected to be significantly less favorable than the sequestered U37-C1 conformation. Assuming 100 $Å^2$ of buried surface area is worth ∼1.5 kcal/mol (*45*) and 1 H-bond is ∼0.48 kcal/mol (*1*), the conformational differences between U37-C1 and U37-C2 of the native structure represent substantial energetic differences. Such heterogeneity must be considered in light of the modest increases in catalytic efficiency reported for the U39C and U39(C3) mutants.

DISCUSSION

Understanding the molecular basis for catalysis by RNA enzymes requires the ability to relate structure to function. Here we report the structure of a minimal, junctionless, all-RNA hairpin ribozyme in a format amenable to chemical synthesis and site directed mutagenesis (Figure 1B). The crystal structure of this bipartite enzyme was solved by molecular replacement (Table 1 and Figure 2) revealing an overall Y-shaped fold (Figure 3A) whose secondary and tertiary elements were preserved with respect to those of the previously determined 4WJ−U1A hairpin ribozyme complex (*22*, *23*). The close agreement of the core RNA folds (Figure 3B) validates the use of a minimal, chemically synthesized hairpin ribozyme as a means to elucidate structure/function relationships that have been limited largely to the nucleotide repertoire of runoff transcription. Likewise, the observation that the 4WJ−U1A structure retained nearly the same core fold as the all-RNA, minimal hairpin ribozyme suggested that the U1A motif does not interfere greatly with the core RNA fold in the context of the crystal lattice. However, the observation of U1A mediated crystal packing interactions to the S-turn (Figure 4A) suggested that solution activity measurements may not be sufficient to gauge the effects of protein incursions in the crystal lattice.

Previously, mutations U39C and U39(C3) were identified by independent studies as "gain-of-function" mutants (*27*−*31*). These studies were conducted in the context of minimal, junctioned hairpin ribozyme constructs that differed from the current study mainly by the presence of a covalent bond between positions 14 and 15 (Figure 1B). Hence, the structure determinations of minimal hairpin ribozymes in this study provide a means to eliminate systematic errors associated with the ribozyme architecture (i.e. minimal versus 4WJ) while leading to the identification of chemical attributes associated with enhanced catalysis. The observation that nucleotide U37 adopted both "exposed" and "sequestered" conformations in the native structure (Figure 4B) implies that heterogeneity normally exists at this position in solution. Significantly, mutations U39C or U39(C3) shifted the conformational equilibrium of U37 toward the sequestered

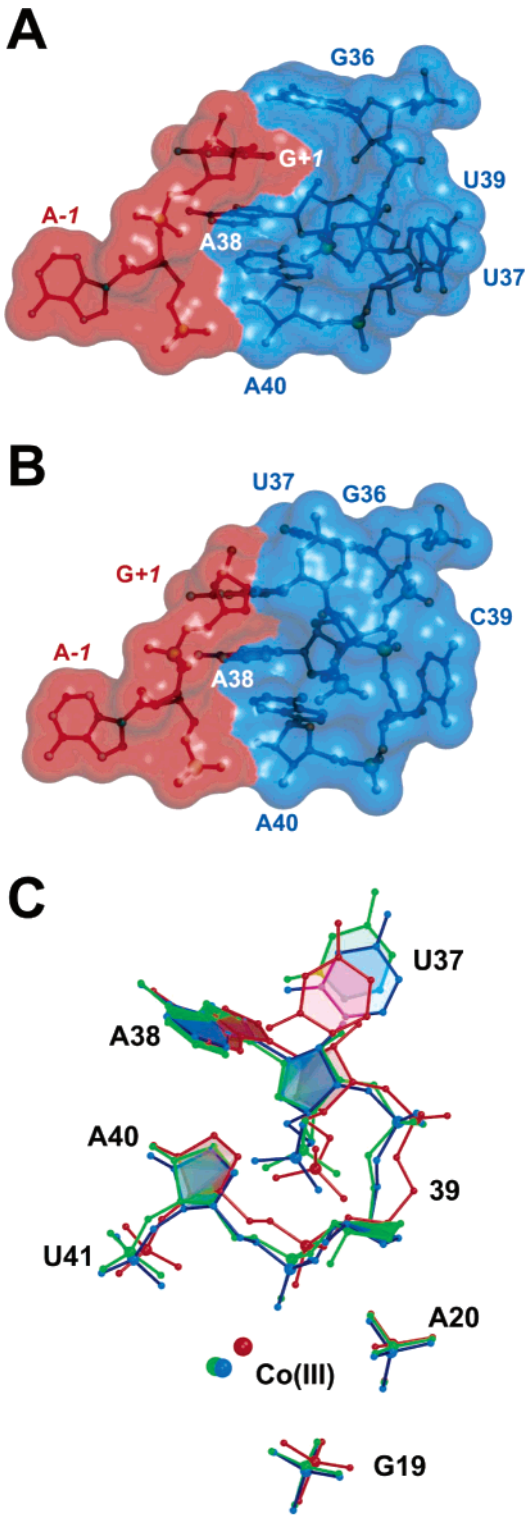

FIGURE 6: Semitransparent surface rendering of the S-turn and triple superposition of metal binding site II. The chains are colored as in Figure 1B. (A) The native minimal hairpin ribozyme structure depicting only the exposed U37-C2 conformation. (B) The U39C mutant of the minimal hairpin ribozyme structure in which U37 adopts a sequestered (C1-like) conformation abutting G+1 and G36. (C) A three-way superposition of the S-turns from the minimal hairpin ribozyme structures of this study. The structures are native (green), U39C mutant (blue), and U39(C3) (red). Cobalt ions without their amine ligands are depicted as spheres. The backbones of positions A19 and G20 are shown for perspective. This view is offset from the other figures for clarity.

state (Figures 4B and 4C). This shift appeared to originate through formation of three new H-bonds for U39C and one new H-bond for U39(C3) (Figures 4E and 4F versus 4G and 4H, respectively), as well as sequestration of ~60 Å^2 compared to the native structure (Figure 6A versus 6B).

To explore the relevance of conformational heterogeneity at position U37, previously reported biochemical experiments were evaluated in light of the new structural information. Chemical modification analysis of G36 suggested that it is generally sequestered from modifying agents (*51*), which indirectly supports the observation of a sequestered conformation for U37 (Figure 6A versus 6B). However, no specific information was reported about the minor groove accessibility of G36, which is most relevant to the current study. In contrast, position U37 has been evaluated in several independent studies. Early reports indicated no loss-of-function when U37 was deleted (*28*, *50*). However, these minimal hairpin ribozyme constructs possessed additional mutations that complicate this conclusion. In contrast, single point mutations conducted at U37 revealed that any base was compatible at this position with less than a 4-fold loss in activity (*49*). This is consistent with the high degree of conformational flexibility observed for U37 in this study (Figures 2A and 4B) suggesting that any base could be accommodated. Strikingly, removal of the U37 base resulted in a 10-fold drop in k_{cat}, supporting a role for base stacking or hydrophobic packing at this position (Figure 6B). Conversely, nearly 8-fold losses in K_M were reported for the respective U37(C3) and 2′-deoxyU37 modifications (*30*), consistent with the observation that the ribose moiety has an important role in interdomain substrate binding (Figure 4B). The latter 2′-deoxyU37 mutation also resulted in a "moderate" deleterious effect ($\Delta\Delta G_{apparent}$ +1.5 kcal/mol) in nucleotide analogue interference mapping (*15*). Although the energy difference exceeds the loss of a single H-bond, the results are consistent with an H-bond between the 2′-OH of U37 and O4′ of G+1 that helps anchor the base in the U37-C1 conformation (Figure 4B). This interaction is notably absent in the exposed, U37-C2 conformation (Figure 4B). Interestingly, chemical modification analysis of the minimal hairpin ribozyme showed that the N1 position of U37 was only moderately susceptible to CMCT, whereas U39 elicited a strong hit for numerous modification agents (*51*). These results seem plausible if U37 remains partly buried in the solution state since the conformation of U37-C2 exhibits nearly the same degree of solvent exposure at its imino group as U39 (Figure 4B).

Further solution studies on the native minimal hairpin ribozyme suggested an important role for the 2′-OH group at position 39. This group points into solution in the 4WJ structure, as well as the U37-C2 conformation of the minimal, native structure (Figures 4A and 4B). Specifically, 2′-deoxy-2′-fluoro-U39 interfered with activity (*15*, *19*), whereas dU39 had only a weak interference effect of 0.6 kcal/mol (*15*), consistent with the loss of a single H-bond. These results are in agreement with the assignment of an H-bond donor at the 2′-OH of position 39 that mediates a contact to the pro-*R* phosphate oxygen of A38 (Figures 4B and 4F). This interaction appears to exist in the mutant and U37-C1 native conformations of the minimal hairpin ribozyme, but not in the U37-C2 conformer of the native or 4WJ structures (Figures 4A and 4E).

Overall, the biochemical data imply that the sequestered, U37-C1 conformation exists in solution with a higher

frequency than that detected in the native hairpin ribozyme structure of this study. This observation seems plausible if one considers (i) that the magnitude of $\Delta\Delta G$ values reported in biochemical studies (above) are consistent with ablation of single H-bonds; (ii) the substantial energetic differences that distinguish the U37-C1 and U37-C2 conformations of the native hairpin ribozyme (i.e. 1 net H-bond and 60 Å^2 of buried area); (iii) the relative net gain of S-turn H-bonds and buried surface area in the structures of the U39C and U39(C3) mutants; and (iv) the fact that only *modest* binding energies were associated with the gain-of-function mutants U39C and U39(C3) mutants (see below). Given this information, it is plausible that conformation U37-C1 represents a precatalytic state, whereas U37-C2 represents an earlier intermediate conformation. If this were so, the energy differences between the precatalytic, native U37-C1 conformation versus the mutant structures could more readily account for the small binding energies associated with their observed increases in relative catalytic efficiency. For example, k_{cat}/K_M (relative) for U39C was ~5.7, whereas that of U39(C3) was ~2.0 (*29*, *30*). This yields changes in relative binding energy ($\Delta\Delta G_{apparent}$) of roughly −1.1 and −0.4 kcal/mol (*30*, *57*), although caution must be exercised since the catalytic efficiencies were obtained from two independent studies conducted on somewhat different minimal hairpin ribozymes. Based upon the structural observations of this study, the net energy difference between the sequestered U37-C1 native versus U39C structures would be nearly −1 kcal/mol (i.e. 2 net H-bonds[2] plus a negligible gain of ~10 Å^2 of buried surface area at U37; Figure 4F versus 4G). In contrast, no net H-bonds are formed in the U39(C3) mutation (Figure 4F versus 4H), so the net energy gained may be attributable to the superior hydrophobic packing of the U37-C1 base (Figure 4D). In the final analysis, the observed structural changes in the S-turn appear to provide a plausible explanation for the gain in catalytic efficiencies of mutants only when comparing their structures to the homogeneous U37-C1 population of the native hairpin ribozyme. This sequestered conformation better accounts for the biochemical studies, as well as the expected differences in binding energy resulting from the U39C and U39(C3) mutations. The origin and significance of the exposed U37-C2 conformation are unclear at this time.

A final aspect of the gain-of-function activities of the respective U39C and U39(C3) mutations was their distinctive metal dependencies. Whereas U39C activated the ribozyme best at <5 mM Mg^{2+} (*29*), the U39(C3) change exhibited little dependence on Mg^{2+} over a 30-fold concentration range (*30*). The observation of a single $Co(NH_3)_6^{3+}$ ion at position G21/A40 (site II, Figure 5B) prompted an analysis of functional studies to assess the relevance of this ion binding site in solution. Position A20 is not conserved phylogenetically (Figure 1B) among hairpin ribozyme sequences (*58*) and can be replaced with any other base without loss of activity (*49*). This is consistent with the rather long H-bond interaction of $Co(NH_3)_6^{3+}$ to N7 of A20 and the nonoptimal coordination geometry (Figure 5B). In fact, replacement of A20 by U or C increases activity ~30% (*49*), which might be explained by the ability of these bases to form a superior coordination sphere for $Mg(H_2O)_6^{2+}$. Conversely, chemical modification studies of the hairpin ribozyme indicated that position G21 becomes strongly protected in the presence of Mg^{2+} ions against NiCR, an N7 base modifier, as well as kethoxal and CMCT (*51*). Backbone cleavage studies with the lanthanide $Tb(OH)(aq)^{2+}$ indicated a strong cleavage hotspot preference at position A20 (*59*). Furthermore, Tb(III) inhibited the hairpin ribozyme cleavage reaction (Figure 1A) in the presence of $Co(NH_3)_6^{3+}$, but inhibition could be reversed by addition of higher concentrations of $Co(NH_3)_6^{3+}$ or Mg^{2+}. These data are consistent with $Co(NH_3)_6^{3+}$ coordination at N7 of G21 and the phosphate backbone of A20 (Figure 5B). Site II was also shown to bind Lu(III) in crystal soaking studies of the high salt 64-mer hairpin ribozyme, but the low resolution data (~3.35 Å resolution) precluded a detailed assignment of the coordination sphere (data not shown). Complementary mutagenesis studies of G21 also suggested an important structural role for this position (*49*). In the crystal structures, the minor groove face of guanine engages in a sheared G·A mismatch with A43 in the E-loop. However, mutation of G21 to O6-methyl guanosine or N7 deazaG reduced catalytic efficiency to 1.2% and 1.7% of native values, corresponding to $\Delta\Delta G_{apparent}$ changes of +2.8 and +2.5 kcal/mol (*60*). Although a detailed analysis of metal binding was not performed in the latter studies, the results appear consistent with the crystal structures of the minimal hairpin ribozymes that show how disruption of metal binding at site II could destabilize core folding interactions at the junction of the E-loop and S-turn.

Previously, the enhanced k_{cat} of U39C under low Mg^{2+} was suggested to be indicative of an improved catalytic center relative to native, possibly as a result of increased metal binding conferred by N3 of C39 (*29*). Although the structures of this study show that C39 points into solvent (Figure 5B), the principle of an improved catalytic center has merit. $Co(NH_3)_6^{3+}$ binding at site II fortifies the S-turn by mediating contacts between A40 and G21 (Figures 3A and 5B). However, new H-bonds in the S-turn and sequestration of residues G36, U37, and G+1 (Figures 4B and 6B) appeared to be the result of the U39C mutation, not metal binding. This is because all three minimal hairpin ribozyme structures were prepared from comparable quantities of $Co(NH_3)_6^{3+}$, yet the conformation of U37 was heterogeneous in the native structure. Furthermore, no detectable structural changes in native and mutant ribozyme structures were observed over a 5-fold range of $Co(NH_3)_6^{3+}$ from 0.1 to 0.5 mM (data not shown). Taken collectively, the preceding data support the idea that the U39C mutation required a lower ion concentration at site II to elicit the same S-turn stabilization as the native hairpin ribozyme. Notably, the site II $Co(NH_3)_6^{3+}$ B-factors of this study indicated the following trend: native (83.2 Å^2) > U39C (51.2 Å^2) > U39(C3) (41.3 Å^2). Indeed, in vitro selection studies indicated that U39C functioned as a second-site suppressor of the strongly inhibitory mutants G21A, G21U, and G21C (*28*) located at the $Co(NH_3)_6^{3+}$ binding site (Figure 5B). The overall impact of a more stable S-turn would be manifest at position A38 (Figure 5B), since proper orientation of this base is necessary for the phosphoryl transfer reaction (*21*).

In contrast to U39C, the U39(C3) mutant exhibited little metal dependence over a 30-fold Mg^{2+} range (*30*). The

[2] The value of a single H-bond was reported to be ~0.48 kcal/mol based on the $\Delta\Delta G_{docking}$ values obtained from removing individual, noncoupled H-bonds from the hairpin ribozyme (*1*).

electron density maps for U39(C3) showed a weak signal for the propyl carbons (Figure 2C), consistent with the inherent flexibility of this substitution. Superpositions of the propyl linker structure upon comparable native and U39C coordinates revealed that the cobalt(III) ion at site II had shifted by nearly 1 Å (Figure 6C). Structural changes were apparent both 5′ to and 3′ of the propyl substitution, including the ribose and phosphate backbone of A38 (Figure 6C). The apparent flexibility of the propyl linker in this region suggests that metal ion binding at site II would have little effect on the adjacent S-turn. This is because the propyl moiety uncouples the metal coordination at U41 and A40 from the upstream structure by acting as a flexible "shock absorber" (Figure 6C). Hence, little benefit would be achieved at the catalytic center despite increasing concentrations of Mg^{2+}.

In summary, the crystal structure of a minimal, junctionless all-RNA hairpin ribozyme has been solved. The core structure is highly homologous to the 4WJ−U1A hairpin ribozyme complexes reported previously (*22*, *23*). As such, this study validates the use of minimal hairpin ribozyme constructs as a means to relate fold to functionally relevant modifications. The native, minimal hairpin ribozyme structure indicated conformational heterogeneity at position U37 comprising both exposed and sequestered forms of the nucleotide. The sequestered form contacts the G+1 ribose moiety forming additional interdomain contacts that concur with previous biochemical studies. Structures of the U39C and U39(C3) mutations appeared to shift the conformational equilibrium of U37 into the sequestered state while providing a structure-based rationale for their differing metal dependencies. Energetic differences between the two conformations of U37, as well as the mutant structures, suggested that the sequestered form of U37 may be relevant to catalysis and that stabilization of the S-turn could influence the sugar/phosphate geometry of the essential catalytic residue A38. Overall, the native and mutant structures demonstrate, at the near atomic level, how coupled molecular motions and H-bond networks can connect distant parts of an RNA enzyme to its active site, which has been invoked previously on a molecular scale (*1*, *31*).

ACKNOWLEDGMENT

The authors are grateful to Nils Walter, C. MacElrevey, and A. Torelli for helpful comments, as well as the staff members of SER-CAT and CHESS for assistance with data collection. CHESS is supported by the NSF under Award DMR-0225180 and NIH through NCRR Award RR-01646. Supporting institutions of SER-CAT may be found at www.ser-cat.org/members.html. Use of the Advanced Photon Source was supported by the U.S. Department of Energy, Office of Science, Office of Basic Energy Sciences, under Contract No. W-31-109-Eng-38.

REFERENCES

1. Klostermeier, D., and Millar, D. P. (2002) Energetics of hydrogen bond networks in RNA: hydrogen bonds surrounding G+1 and U42 are the major determinants for the tertiary structure stability of the hairpin ribozyme, *Biochemistry 41*, 14095−102.
2. McKay, D. B., and Wedekind, J. E. (1999) in *The RNA World* (Cech, T., Ed.) pp 265−286, Cold Spring Harbor Laboratory Press, Cold Spring Harbor.
3. Winkler, W. C., Nahvi, A., Roth, A., Collins, J. A., and Breaker, R. R. (2004) Control of gene expression by a natural metabolite-responsive ribozyme, *Nature 428*, 281−6.
4. Doherty, E. A., and Doudna, J. A. (2001) Ribozyme structures and mechanisms, *Annu. Rev. Biophys. Biomol. Struct. 30*, 457−75.
5. Doudna, J. A., and Lorsch, J. R. (2005) Ribozyme catalysis: not different, just worse, *Nat. Struct. Mol. Biol. 12*, 395−402.
6. Fedor, M. J., and Williamson, J. R. (2005) The catalytic diversity of RNAs, *Nat. Rev. Mol. Cell. Biol. 6*, 399−412.
7. Buzayan, J. M., Hampel, A., and Bruening, G. (1986) Nucleotide sequence and newly formed phosphodiester bond of spontaneously ligated satellite tobacco ringspot virus RNA, *Nucleic Acids Res. 14*, 9729−43.
8. Murchie, A. I., Thomson, J. B., Walter, F., and Lilley, D. M. (1998) Folding of the hairpin ribozyme in its natural conformation achieves close physical proximity of the loops, *Mol. Cell 1*, 873−81.
9. Hampel, A., and Tritz, R. (1989) RNA catalytic properties of the minimum (-)sTRSV sequence, *Biochemistry 28*, 4929−33.
10. Butcher, S. E., Heckman, J. E., and Burke, J. M. (1995) Reconstitution of hairpin ribozyme activity following separation of functional domains, *J. Biol. Chem. 270*, 29648−51.
11. Shin, C., Choi, J. N., Song, S. I., Song, J. T., Ahn, J. H., Lee, J. S., and Choi, Y. D. (1996) The loop B domain is physically separable from the loop A domain in the hairpin ribozyme, *Nucleic Acids Res. 24*, 2685−9.
12. Earnshaw, D. J., Masquida, B., Muller, S., Sigurdsson, S. T., Eckstein, F., Westhof, E., and Gait, M. J. (1997) Inter-domain cross-linking and molecular modelling of the hairpin ribozyme, *J. Mol. Biol. 274*, 197−212.
13. Shippy, R., Siwkowski, A., and Hampel, A. (1998) Mutational analysis of loops 1 and 5 of the hairpin ribozyme, *Biochemistry 37*, 564−70.
14. Pinard, R., Lambert, D., Walter, N. G., Heckman, J. E., Major, F., and Burke, J. M. (1999) Structural basis for the guanosine requirement of the hairpin ribozyme, *Biochemistry 38*, 16035−9.
15. Ryder, S. P., and Strobel, S. A. (1999) Nucleotide Analog Interference Mapping of the Hairpin Ribozyme: Implications for Secondary and Tertiary Structure Formation, *J. Mol. Biol. 291*, 295−311.
16. Porschke, D., Burke, J. M., and Walter, N. G. (1999) Global structure and flexibility of hairpin ribozymes with extended terminal helices, *J. Mol. Biol. 289*, 799−813.
17. Pinard, R., Hampel, K. J., Heckman, J. E., Lambert, D., Chan, P. A., Major, F., and Burke, J. M. (2001) Functional involvement of G8 in the hairpin ribozyme cleavage mechanism, *EMBO J. 20*, 6434−42.
18. Lebruska, L. L., Kuzmine, II, and Fedor, M. J. (2002) Rescue of an abasic hairpin ribozyme by cationic nucleobases: evidence for a novel mechanism of RNA catalysis, *Chem. Biol. 9*, 465−73.
19. Ryder, S. P., and Strobel, S. A. (2002) Comparative analysis of hairpin ribozyme structures and interference data, *Nucleic Acids Res. 30*, 1287−91.
20. Fedor, M. J. (2000) Structure and function of the hairpin ribozyme, *J. Mol. Biol. 297*, 269−91.
21. Kuzmin, Y. I., Da Costa, C. P., and Fedor, M. J. (2004) Role of an active site guanine in hairpin ribozyme catalysis probed by exogenous nucleobase rescue, *J. Mol. Biol. 340*, 233−51.
22. Rupert, P. B., and Ferre-D'Amare, A. R. (2001) Crystal structure of a hairpin ribozyme-inhibitor complex with implications for catalysis, *Nature 410*, 780−6.
23. Rupert, P. B., Massey, A. P., Sigurdsson, S. T., and Ferre-D'Amare, A. R. (2002) Transition state stabilization by a catalytic RNA, *Science 298*, 1421−4.
24. Bevilacqua, P. C. (2003) Mechanistic considerations for general acid-base catalysis by RNA: revisiting the mechanism of the hairpin ribozyme, *Biochemistry 42*, 2259−65.
25. Ferre-D'Amare, A. R. (2004) The hairpin ribozyme, *Biopolymers 73*, 71−8.
26. Kuzmin, Y. I., Da Costa, C. P., Cottrell, J. W., and Fedor, M. J. (2005) Role of an active site adenine in hairpin ribozyme catalysis, *J. Mol. Biol. 349*, 989−1010.
27. Berzal-Herranz, A., Joseph, S., and Burke, J. M. (1992) In vitro selection of active hairpin ribozymes by sequential RNA-catalyzed cleavage and ligation reactions, *Genes Dev. 6*, 129−34.
28. Berzal-Herranz, A., Joseph, S., Chowrira, B. M., Butcher, S. E., and Burke, J. M. (1993) Essential nucleotide sequences and secondary structure elements of the hairpin ribozyme, *EMBO J. 12*, 2567−73.

29. Joseph, S., and Burke, J. M. (1993) Optimization of an anti-HIV hairpin ribozyme by in vitro selection, *J. Biol. Chem. 268*, 24515−8.
30. Schmidt, S., Beigelman, L., Karpeisky, A., Usman, N., Sorensen, U. S., and Gait, M. J. (1996) Base and sugar requirements for RNA cleavage of essential nucleoside residues in internal loop B of the hairpin ribozyme: implications for secondary structure, *Nucleic Acids Res. 24*, 573−81.
31. Rueda, D., Bokinsky, G., Rhodes, M. M., Rust, M. J., Zhuang, X., and Walter, N. G. (2004) Single-molecule enzymology of RNA: essential functional groups impact catalysis from a distance, *Proc. Natl. Acad. Sci. U.S.A. 101*, 10066−71.
32. Grum-Tokars, V., Milovanovic, M., and Wedekind, J. E. (2003) Crystallization and X-ray diffraction analysis of an all-RNA U39C mutant of the minimal hairpin ribozyme, *Acta Crystallogr. D 59*, 142−5.
33. Hampel, K. J., Walter, N. G., and Burke, J. M. (1998) The solvent-protected core of the hairpin ribozyme-substrate complex, *Biochemistry 37*, 14672−82.
34. Wedekind, J. E., and McKay, D. B. (2000) Purification, crystallization, and X-ray diffraction analysis of small ribozymes, *Methods Enzymol. 317*, 149−68.
35. Pflugrath, J. W. (1999) The finer things in X-ray diffraction data collection, *Acta Crystallogr. D 55*, 1718−25.
36. Navaza, J. (2001) Implementation of molecular replacement in AMoRe, *Acta Crystallogr. D 57*, 1367−72.
37. Brünger, A. T., Adams, P. D., Clore, G. M., DeLano, W. L., Gros, P., Grosse-Kunstleve, R. W., Jiang, J. S., Kuszewski, J., Nilges, M., Pannu, N. S., Read, R. J., Rice, L. M., Simonson, T., and Warren, G. L. (1998) Crystallography & NMR system: A new software suite for macromolecular structure determination, *Acta Crystallogr. D 54*, 905−21.
38. Jones, T. A., Zou, J. Y., Cowan, S. W., and Kjeldgaard, M. (1991) Improved methods for building protein models in electron density maps and the location of errors in these models, *Acta Crystallogr. A 47*, 110−9.
39. Collaborative Computational Project, Number 4 (1994) The CCP4 Suite: Programs for Protein Crystallography, *Acta Crystallogr. D 50*, 760−3.
40. Esnouf, R. M. (1999) Further additions to MolScript version 1.4, including reading and contouring of electron-density maps, *Acta Crystallogr. D 55*, 938−40.
41. DeLano, W. L. (2002) *The PyMOL Molecular Graphics System*, DeLano Scientific, San Carlos, California.
42. Pley, H. W., Flaherty, K. M., and McKay, D. B. (1994) Three-dimensional structure of a hammerhead ribozyme, *Nature 372*, 68−74.
43. Cate, J. H., Gooding, A. R., Podell, E., Zhou, K., Golden, B. L., Kundrot, C. E., Cech, T. R., and Doudna, J. A. (1996) Crystal structure of a group I ribozyme domain: principles of RNA packing, *Science 273*, 1678−85.
44. Dunham, C. M., Murray, J. B., and Scott, W. G. (2003) A helical twist-induced conformational switch activates cleavage in the hammerhead ribozyme, *J. Mol. Biol. 332*, 327−36.
45. Vallone, B., Miele, A. E., Vecchini, P., Chiancone, E., and Brunori, M. (1998) Free energy of burying hydrophobic residues in the interface between protein subunits, *Proc. Natl. Acad. Sci. U.S.A. 95*, 6103−7.
46. Correll, C. C., Freeborn, B., Moore, P. B., and Steitz, T. A. (1997) Metals, motifs, and recognition in the crystal structure of a 5S rRNA domain, *Cell 91*, 705−12.
47. Tamura, M., and Holbrook, S. R. (2002) Sequence and structural conservation in RNA ribose zippers, *J. Mol. Biol. 320*, 455−74.
48. Klostermeier, D., and Millar, D. P. (2001) Tertiary structure stability of the hairpin ribozyme in its natural and minimal forms: different energetic contributions from a ribose zipper motif, *Biochemistry 40*, 11211−8.
49. Siwkowski, A., Shippy, R., and Hampel, A. (1997) Analysis of hairpin ribozyme base mutations in loops 2 and 4 and their effects on cis-cleavage in vitro, *Biochemistry 36*, 3930−40.
50. Anderson, P., Monforte, J., Tritz, R., Nesbitt, S., Hearst, J., and Hampel, A. (1994) Mutagenesis of the hairpin ribozyme, *Nucleic Acids Res. 22*, 1096−100.
51. Butcher, S. E., and Burke, J. M. (1994) Structure-mapping of the hairpin ribozyme. Magnesium-dependent folding and evidence for tertiary interactions within the ribozyme-substrate complex, *J. Mol. Biol. 244*, 52−63.
52. Young, K. J., Gill, F., and Grasby, J. A. (1997) Metal ions play a passive role in the hairpin ribozyme catalysed reaction, *Nucleic Acids Res. 25*, 3760−6.
53. Nesbitt, S., Hegg, L. A., and Fedor, M. J. (1997) An unusual pH-independent and metal-ion-independent mechanism for hairpin ribozyme catalysis, *Chem. Biol. 4*, 619−30.
54. Fedor, M. J. (2002) The role of metal ions in RNA catalysis, *Curr. Opin. Struct. Biol. 12*, 289−95.
55. Hingerty, B. E., Brown, R. S., and Klug, A. (1982) Stabilization of the tertiary structure of yeast phenylalanine tRNA by $[Co(NH_3)_6]^{3+}$. X-ray evidence for hydrogen bonding to pairs of guanine bases in the major groove, *Biochim. Biophys. Acta 697*, 78−82.
56. Hakoshima, T., Omori, H., Tomita, K., Miki, H., and Ikehara, M. (1981) The crystal and molecular structure of 2′-deoxy-2′-fluoroinosine monohydrate, *Nucleic Acids Res. 9*, 711−29.
57. Fersht, A. R. (1999) *Structure and Mechanism in Protein Science: A guide to enzyme catalysis and protein folding*, W. H. Freeman and Company, New York.
58. DeYoung, M., Siwkowski, A. M., Lian, Y., and Hampel, A. (1995) Catalytic properties of hairpin ribozymes derived from Chicory yellow mottle virus and arabis mosaic virus satellite RNAs, *Biochemistry 34*, 15785−91.
59. Walter, N. G., Yang, N., and Burke, J. M. (2000) Probing non-selective cation binding in the hairpin ribozyme with Tb(III), *J. Mol. Biol. 298*, 539−55.
60. Grasby, J. A., Mersmann, K., Singh, M., and Gait, M. J. (1995) Purine functional groups in essential residues of the hairpin ribozyme required for catalytic cleavage of RNA, *Biochemistry 34*, 4068−76.
61. Yang, H., Jossinet, F., Leontis, N., Chen, L., Westbrook, J., Berman, H., and Westhof, E. (2003) Tools for the automatic identification and classification of RNA base pairs, *Nucleic Acids Res. 31*, 3450−60.

BI051550I